ACS APPLIED NANO MATERIALS

www.acsanm.org Article

Influence of Lithium Doping on Volcanic-like Perovskite Memristors and Artificial Synaptic Simulation for Neurocomputing

Juan Gao, Qin Gao,* Jiangshun Huang, Xiaoyue Feng, Xueli Geng, Haoze Li, Guoxing Wang, Bo Liang, Xueliang Chen, Yuanzhao Su, Mei Wang, Zhisong Xiao, Paul K. Chu, and Anping Huang*

Cite This: *ACS Appl. Nano Mater.* 2023, 6, 7975−7983 Read Online

ACCESS | Metrics & More | Article Recommendations | Supporting Information

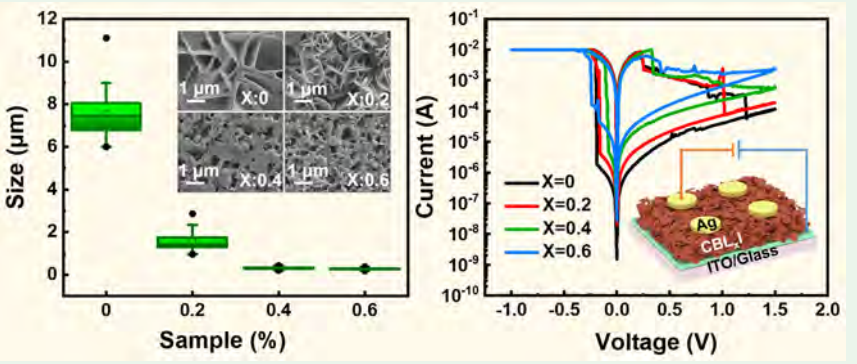

ABSTRACT: Perovskite-based memristors have attracted much attention in synaptic simulation due to their outstanding electrical properties and promising potential in neuromorphic computing (NC). In this work, inorganic lead-free perovskite-based memristors composed of Ag/$Cs_3Bi_{2-x}Li_xI_{9-2x}$ (CBL_xI)/ITO (x = 0, 0.2, 0.4, 0.6) are fabricated, and the electrical properties, such as endurance, on/off ratio, and retention time, are determined. It is found that the device with x = 0.4 shows good characteristics, such as a set voltage of −0.1 V and a retention time of 10^4 s. The multilevel storage performance is investigated, and multiple synaptic characteristics, such as paired-pulse facilitation (PPF), spike-voltage-dependent plasticity (SVDP), spike-width-dependent plasticity (SWDP), spike-timing-dependent plasticity (STDP), and learning−forgetting, are simulated. The conductive mechanism of the device is analyzed and discussed with an analogy to natural volcanic rocks, which also have a large surface area, high adsorption, and high chemical inertness. An artificial neural network (ANN) based on the potentiation/depression characteristics is designed and analyzed theoretically, and a pattern recognition rate of 94.25% is accomplished. The strategy and results described in this paper provide insights into the development of nonvolatile memory devices boding well for the adoption of neuromorphic computing for image recognition.

KEYWORDS: *perovskite, lithium Ions, synaptic plasticity, synaptic memristor, neurocomputing*

INTRODUCTION

In recent years, rapid progress has been made in the application of perovskites to electronic devices, such as memristors and artificial synaptic devices, due to the ion migration characteristics and manufacturing advantages. In particular, the mixed ionic−electronic conduction behavior found in perovskite-based memristors provides the possibility to simulate the synaptic functions for neuromorphic computing (NC).[1−5] Perovskites are mainly divided into organic−inorganic halide perovskites (OHPs) and all-inorganic perovskites (APs). The high moisture absorption of organic cations in OHPs and the toxicity of lead in OHPs and APs restrict the large-scale application to NC.[6−12] Due to the low toxicity and high environmental stability, inorganic lead-free perovskite-based memristors have attracted extensive attention.[13−16] However, the low-dimensional characteristics of inorganic lead-free perovskites give rise to poor film formation and inferior charge transport, which may reduce the durability and fatigue resistance of perovskite-based memristors.[17−20] New design,[21,22] interfacial engineering,[23] and elemental doping[24] have been proposed to control conductive filament formation and improve the device properties. For example, Paramanik et al. have prepared $Cs_3Sb_2I_9$ perovskite-based memristors by a vapor-assisted solution technique, achieved a retention time of 10^4 s and an endurance of over

Received: March 17, 2023
Accepted: April 23, 2023
Published: May 3, 2023

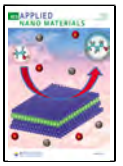

Scheme 1. Schematic of the Synthesis of the Ag/CBL_xI (x = 0, 0.2, 0.4, 0.6)/ITO Devices

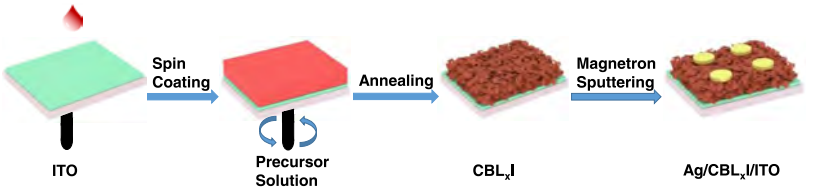

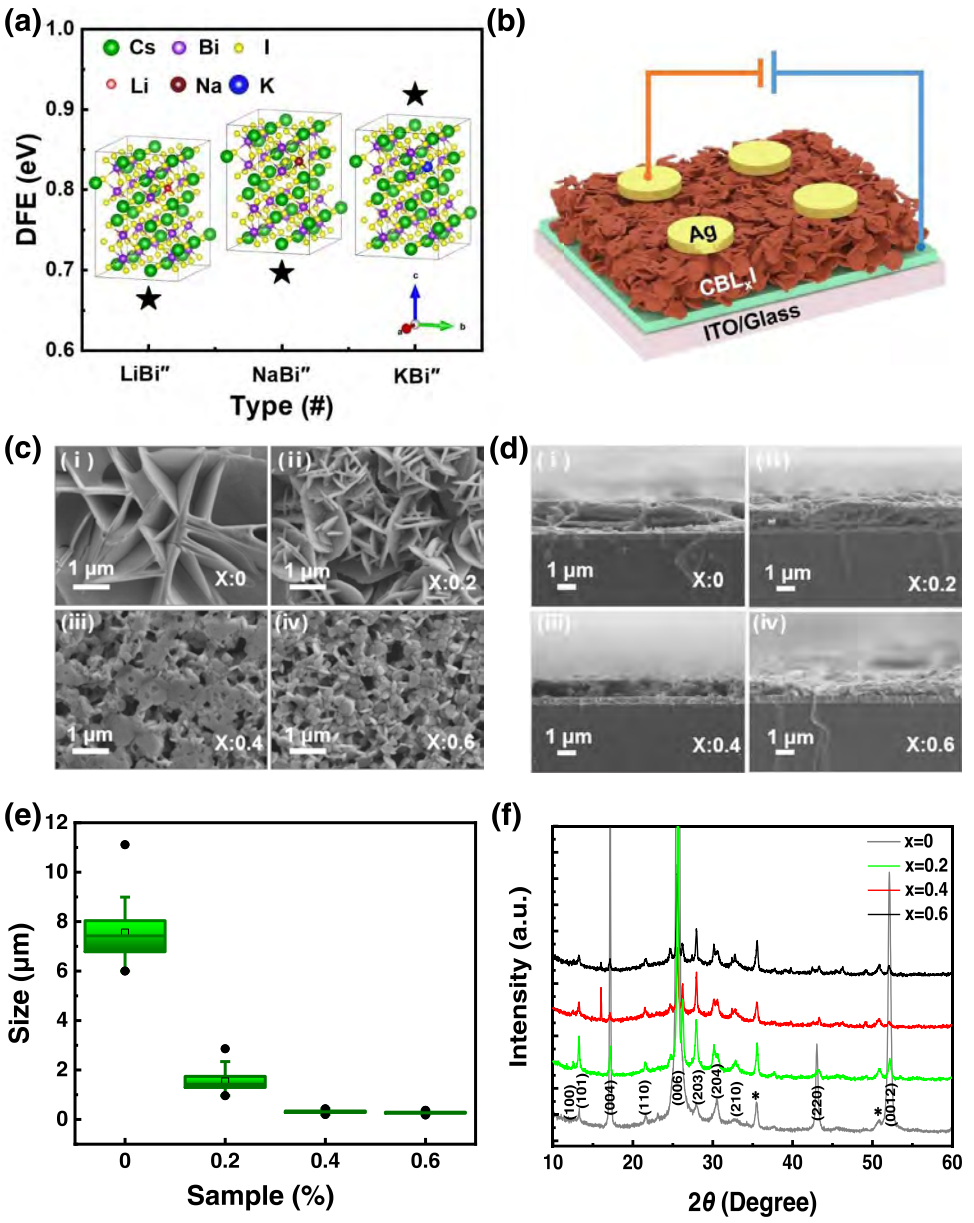

Figure 1. (a) DFE images of Li, Na, and K replacing Bi in CBI; (b) schematic diagram of the Ag/CBL_xI/ITO synapse memristor; (c) surface and (d) cross-sectional SEM images of CBL_xI ((i) x = 0, (ii) x = 0.2, (iii) x = 0.4, and (iv) x = 0.6); (e) box−whisker plots of the perovskite grain sizes for different dopant concentrations; and (f) XRD patterns of the perovskite films with different dopant concentrations.

100 cycles, and simulated the basic synaptic properties, such as STP and LTP.[25] Sheng et al. have improved the reliability by introducing AIZS QDs into the heterojunction with $Cs_3Cu_2Cl_5$ and conducted synaptic simulation.[23] Jang et al. have prepared the dual-phase $(Cs_3Bi_2I_9)_{0.4}$−$(CsPbI_3)_{0.6}$ perovskite device by doping with Bi to improve the durability.[26] Doping can also be used to change the morphology of films and provide more sites for ion storage.[27] In addition, natural biomimetic structures have been proposed to improve the stability, on−off ratio, and retention time. For instance, a karst-like biomimetic device has been designed to regulate ion transport and improve memristive characteristics.[28]

In this work, CBL_xI (x = 0, 0.2, 0.4, 0.6) perovskite films are fabricated by the solution method and the morphology is regulated by doping with different amounts of lithium. The memristive properties are determined systematically. The set

https://doi.org/10.1021/acsanm.3c01203
ACS Appl. Nano Mater. 2023, 6, 7975−7983

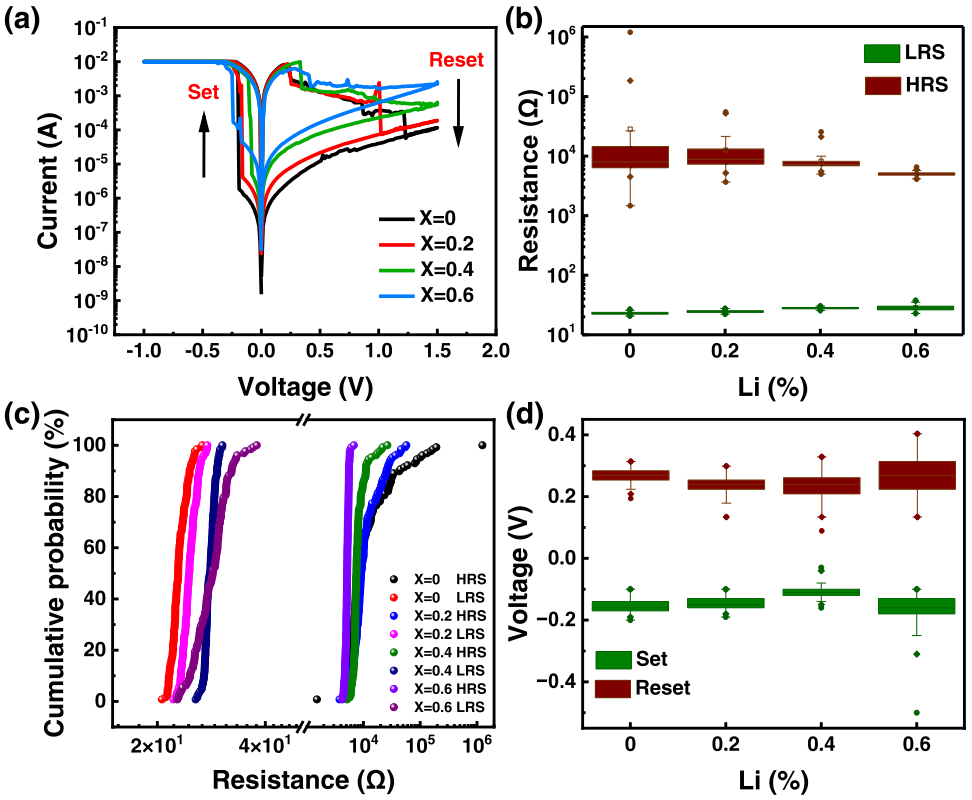

Figure 2. (a) $I-V$ curves of Ag/CBL$_x$I (x = 0, 0.2, 0.4, 0.6)/ITO; (b) statistical data of the HRS/LRS of CBL$_x$I (x = 0, 0.2, 0.4, and 0.6) depicted by the box−whisker plots; (c) cumulative probabilities of the HRS/LRS of CBL$_x$I (x = 0, 0.2, 0.4, 0.6)-based devices; and (d) statistical data of the set/reset voltages of CBL$_x$I (x = 0, 0.2, 0.4, and 0.6) depicted by the box−whisker plots.

voltage is as low as −0.1 V, and the retention time is about 10^4 s for the device with x = 0.4. The multilevel storage properties and synaptic functions are simulated, and the accuracy of pattern recognition is determined. The conductive mechanism of ion migration is discussed based on the analogy with volcanic rocks in nature. This study reveals the high potential of the concept and materials in artificial synaptic devices and their application to pattern recognition and NC.

EXPERIMENTAL METHODS

Preparation of CBL$_x$I film. The CBL$_x$I (x = 0, 0.2, 0.4, 0.6) perovskite films were prepared by spin coating. The ITO-coated glass substrates were cleaned ultrasonically in acetone, ethanol, and distilled water for 15 min each and dried with nitrogen. LiI (Aladdin; 99.99%; 0, 0.13, 0.25, and 0.38 mmol) was mixed with CsI (Aladdin, 99.999%) and BiI_3 (Aladdin, 99.99%) and dissolved in dimethylformamide (DMF) (Innochem, 99.9%) to produce the CBL$_x$I (x = 0, 0.2, 0.4, and 0.6) perovskite precursor solution with a concentration of 0.31 mol/L. The precursor solution was sonicated for 3 h and heated at 70 °C for 24 h. The solution was spin-coated onto the ITO substrates at 500 rpm for 15 s and then 3000 rpm for 60 s to improve the film quality before annealing at 100 °C for 15 min.

Preparation of the Ag/CBL$_x$I/ITO Device. An Ag (~240 nm) top electrode was prepared on CBL$_x$I/ITO by direct current (DC) magnetron sputtering. The electrode diameter was 500 μm, the sputtering power was 80 W, the pressure was 6×10^{-4} Pa, and the Ar flow rate was 30 sccm. The cross section of the Ag/CBL$_{0.4}$I/ITO stacks is shown in Figure S1, and the synthetic route is shown in Scheme 1.

Characterization. The morphology of the device was examined by SEM, and the electrical properties were determined on a Keithley 4200 semiconductor parameter analyzer and an AFG31000 series arbitrary function generator.

RESULTS AND DISCUSSION

The defect formation energies (DFEs) of the CBI perovskite samples with alkali metals (Li, Na, K) replacing Bi are first determined by first-principles calculation as shown in Figure 1a. The inset in Figure 1a shows the crystal structure with different alkali ions. The DFE of Bi replaced by Li is 0.66 eV, which is lower than Na and K substitution of 0.70 and 0.92 eV, respectively. In addition, the DFE of Cs replaced by Li is 1.46 eV, indicating that Li can easily substitute for Bi, as shown in Table S1. The structure of the Ag/CBL$_x$I/ITO device is presented in Figure 1b. The SEM images of the perovskite layer with different lithium concentrations are shown in Figure 1c,d, respectively. Without Li doping (x = 0), the surface appears as a grid with large particle intersections and large and deep pore areas, as shown in Figures 1c−i and 1d−i. As the dopant concentrations increase, the size of the perovskite grain and hole decreases as shown in Figure 1c-ii, c-iv, and 1d-ii−d-iv. The grain size of the films is analyzed statistically as shown in Figures 1e and S2. With increasing dopant concentration, the surface roughness decreases first and then increases, as shown in Figure S3. During crystal growth, Li ions can act as the nucleation sites and cause the Zener pinning effect,[29,30] which decreases the grain size sharply and then stabilizes when the dopant concentration goes up, as shown in Figure 1e. When the doping concentration is x = 0.6, the grain size is similar to that of x = 0.4, but there are more pores and the surface is rougher due to the high Lewis acidity of lithium halide. The crystallization rate of the perovskite increases gradually with dopant concentration producing more holes in the films.[31,32] The perovskite thin films with different lithium concentrations are analyzed by XRD as shown in Figure 1f.

https://doi.org/10.1021/acsanm.3c01203
ACS Appl. Nano Mater. 2023, 6, 7975−7983

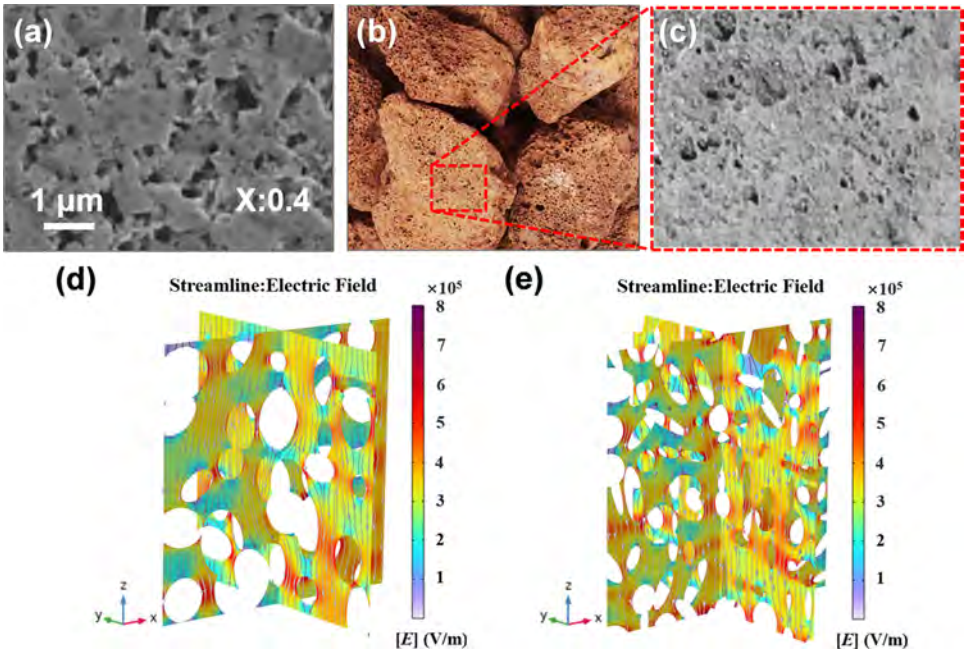

Figure 3. (a) SEM images of $CBL_{0.4}I$, (b) volcanic rock structure in nature, and (c) partial enlarged drawing. The three-dimensional electric field simulation of (d) larger porous structure and (e) smaller porous structure.

The CBL_xI (x = 0, 0.2, 0.4, 0.6) perovskite films have a hexagonal crystal structure and preferred orientation along the (006) direction. Some other low-intensity diffraction peaks are observed, suggesting that the crystal orientation is random.[19,33]

The $I-V$ characteristics of the Ag/CBL_xI/ITO devices are determined in the voltage sweeping direction of 0 → −1 → 0 → 1.5 → 0 V, as shown in Figure 2a. When the voltage is scanned from 0 to −1 V, the device changes from a high resistance state (HRS) to a low resistance state (LRS), which represents the set process. After this transition, the LRS remains until the positive bias voltage is changed from 0 to 1.5 V, in which case the resistance state returns to the HRS, corresponding to the reset process. The endurance test is shown in Figure S4a−d, and the on/off ratios are presented statistically in Figure S4e−h. The HRS of the devices decreases gradually with dopant concentration, as shown in Figure 2b. This is due to the increase in the iodine vacancy (V_I) concentration in the perovskite films as the dopant concentration is increased. According to the endurance statistics of the device, the cumulative probability of the device is analyzed for 128 cycles as shown in Figure 2c. As the dopant concentration increases, the stability of the resistance state cycle improves. The grain size and grain boundary distribution of the perovskite films have a large influence on the resistance. When the grain size is large, the migration path of V_I is disordered resulting in instability. A higher Li concentration decreases the grain size, and the grain boundaries become denser, making ion migration more stable.[34−36] The set/reset voltage of the devices with different Li-ion concentrations is shown in Figure 2d. The set/reset voltage of the device decreases when the Li dopant concentration is x = 0, 0.2, and 0.4, respectively, and then increases when x = 0.6. The resistance is mainly caused by the formation and fracture of the V_I conductive filament (CF).[19,36−39] The larger holes can drive a higher internal electric field, and a large external electric field is required to drive ion migration. Therefore, the required operating voltage decreases as the aperture decreases.[40] In addition, a higher V_I is generated as the concentration of lithium increases, and it may also cause the operating voltage to decrease. However, when the dopant concentration is x = 0.6, operating voltage surges occur because excessive Li ions accumulate in the lattice gap and grain boundaries to hinder the migration of V_I. Figure S4i−l shows the retention time of the devices, and the $CBL_{0.4}I$-based devices exhibit a longer retention time of up to 10^4 s.

Figure 3a discloses that the $CBL_{0.4}I$-based perovskite film has a micro-/nanoporous structure similar to that of natural volcanic rocks shown in Figure 3b. Figure 3c shows the local enlargement of Figure 3b. In nature, volcanic rocks have a large surface area and high adsorption, and the abundant pores provide sites for microbial adhesion and facilitate their growth.[41] The charged properties of porous perovskite structures are similar to the functions of volcanic rocks, which can attract iodine ions to adhere to the channel wall. Positive ions closer to the channel wall are attracted by the stronger force, and hence, the pores in the perovskite layer can relieve the electro-osmotic flow to facilitate long-term storage of V_I and improve the stability of the device.

The three-dimensional field effect density distribution map is simulated by COMSOL Multiphysics software as shown in Figure 3d,e. The structure with larger pores has a weaker electric field as shown in Figure 3d compared to Figure 3e, which shows mixed micro-/nanopores. The log (I)−log (V) data are analyzed to explain the mechanisms of the CBL_xI-based perovskite device as shown in Figure S5 (Supporting Information). To further demonstrate that the resistance is dominated by the formation and fracture of the V_I CF, the influence of different electrode areas and electrode materials, such as Pt, Au Ag, and Cu, is analyzed and shown in Figure S6 (Supporting Information). In addition, the resistance stability is compared with that of other perovskite materials in Figure S7a in the Supporting Information. C_{HRS} and C_{LRS} represent the coefficients of variations of HRS and LRS, respectively. The formula is $C = \sigma/\mu$,[42] where σ is the resistance standard

https://doi.org/10.1021/acsanm.3c01203
ACS Appl. Nano Mater. 2023, 6, 7975−7983

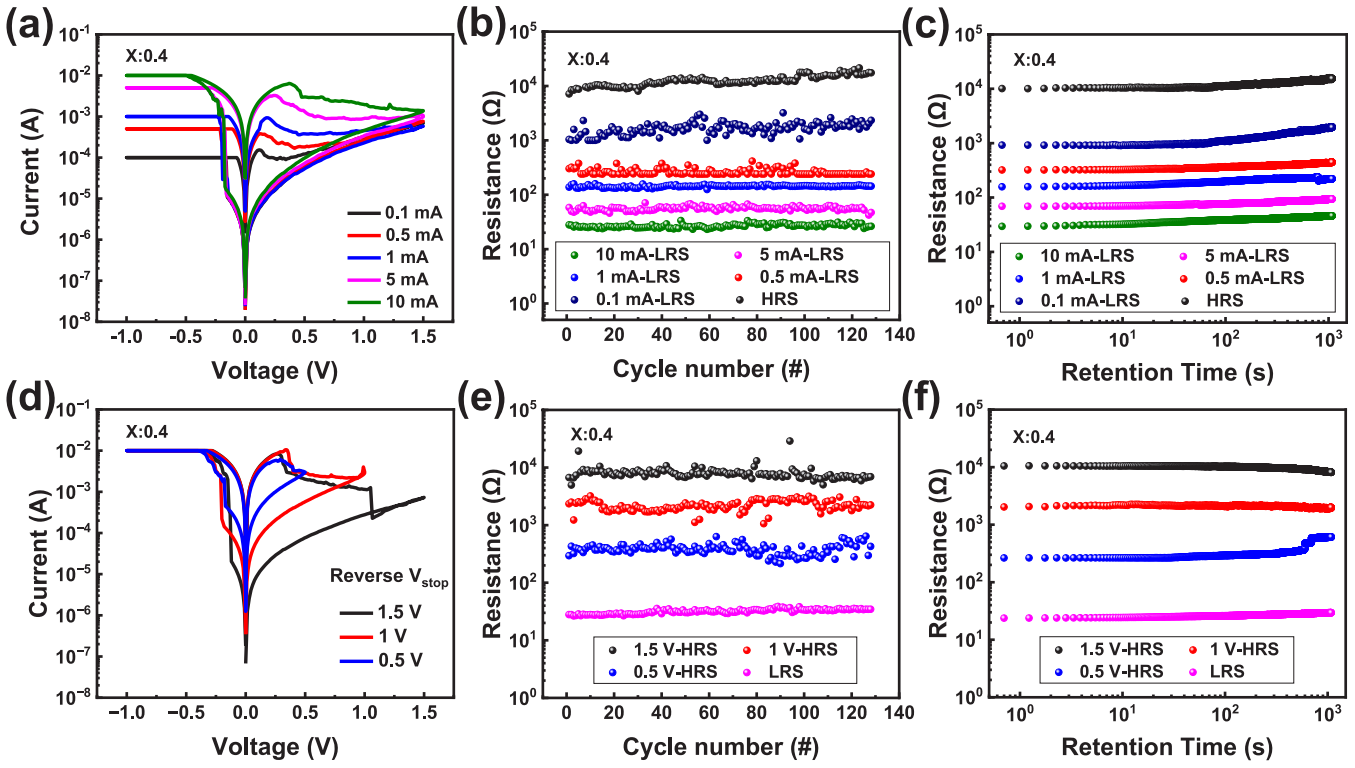

Figure 4. Multilevel memory characteristics studied by applying different I_{cc}: (a) Multilevel $I-V$ characteristics, (b) multilevel endurance, and (c) multilevel retention. Multilevel memory characteristics studied by applying different V_{reset}: (d) multilevel $I-V$ characteristics, (e) multilevel endurance, and (f) multilevel retention.

deviation and μ is the mean value, and the relevant data comparison is shown in Figures S7b,c. In comparison with other devices reported in the literature shown in Table S2, our device has advantages in terms of the operating voltage, retention time, and other memristive properties.

Multilevel storage is an important characteristic for memristors and NC. The multilevel memory characteristics are studied by applying different compliance current (I_{cc}) and V_{reset}. Five resistance states with different I_{cc} can be clearly identified, as shown in Figure 4a. The results show that the HRS is independent of I_{cc}, and the LRS increases with increasing I_{cc}, forming five levels of LRS (10, 5, 1, 0.5, and 0.1 mA). I_{cc} affects the robustness of CF consistent with other studies.[43] Figure 4b shows that the endurance of HRS and five levels of LRS, which can clearly distinguish the five different resistance states for different I_{cc} values. The retention time of 10^3 s is completed for different I_{cc} values as shown in Figure 4c. Figure 4d shows the multilevel $I-V$ characteristics by applying the same set voltage (−1 V) and different reset voltages (0.5, 1, and 1.5 V). Four distinguishable resistance states are obtained, including LRS and 3 levels of HRS (0.5, 1, and 1.5 V). It is worth noting that a high reset voltage implies reduction in residual CF and higher HRS. The endurance test and retention time are determined according to the different reset voltages shown in Figure 4e,f, respectively. Consecutive positive and negative voltage scans are performed, and the $V-t$ and $I-t$ curves in Figure S8 show the cumulative memory effects with increasing (0 to −0.025 V)/decreasing (0 to 1.2 V) voltages.

Based on the memristive properties in the direct current test, the synaptic plasticity simulation is performed according to the functions of biological synaptic systems. In our device, the top and bottom electrodes can be regarded as the synaptic presynaptic membrane used as the signal input terminal, whereas the postsynaptic membrane is employed as the signal output terminal. The middle perovskite layer can be regarded as the synaptic cleft and the conductance change of the middle perovskite layer is considered the synaptic weight as shown in Figure 5a. Figure 5b presents the full memristor-based artificial circuit. The potentiation/depression operation is performed for 200 set pulses (−0.3 V, 600 μs), followed by 200 reset pulses (0.3 V, 600 μs) shown in Figure 5c. When consecutive negative electrical pulses are applied, V_I migrates toward the Ag electrode, the CF grows to ITO, and the gap between the CF and ITO electrode decreases, thus increasing the synaptic weight. As a reverse bias is applied, V_I migrates toward the ITO electrode to produce a larger gap between the CF and ITO for synaptic inhibition.[20] Here, the conductance changes are plotted against synaptic weights. The short-term plasticity (STP) and long-term plasticity (LTP) are important properties of synapses related to learning and memory and are simulated in our work. Paired-pulse facilitation (PPF) is a typical feature of STP and depends on the time interval between two consecutive pulses. Two consecutive pulses are applied to the device, and the current peak generated by the first pulse stimulation is defined as I_1. The current peak generated by the second pulse stimulation is defined as I_2, and the double-pulse facilitation gain is expressed by the following formula[44]

$$\mathrm{PPF}\% = (I_2 - I_1)/I_1 \times 100\% \quad (1)$$

The pulse amplitude is −0.3 V, and the time interval between two consecutive pulses is from 100 to 1000 μs. As the time interval between two pulses increases, the PPF value drops from 23.2 to 0.6% as shown in Figure 5d. The double-

https://doi.org/10.1021/acsanm.3c01203
ACS Appl. Nano Mater. 2023, 6, 7975−7983

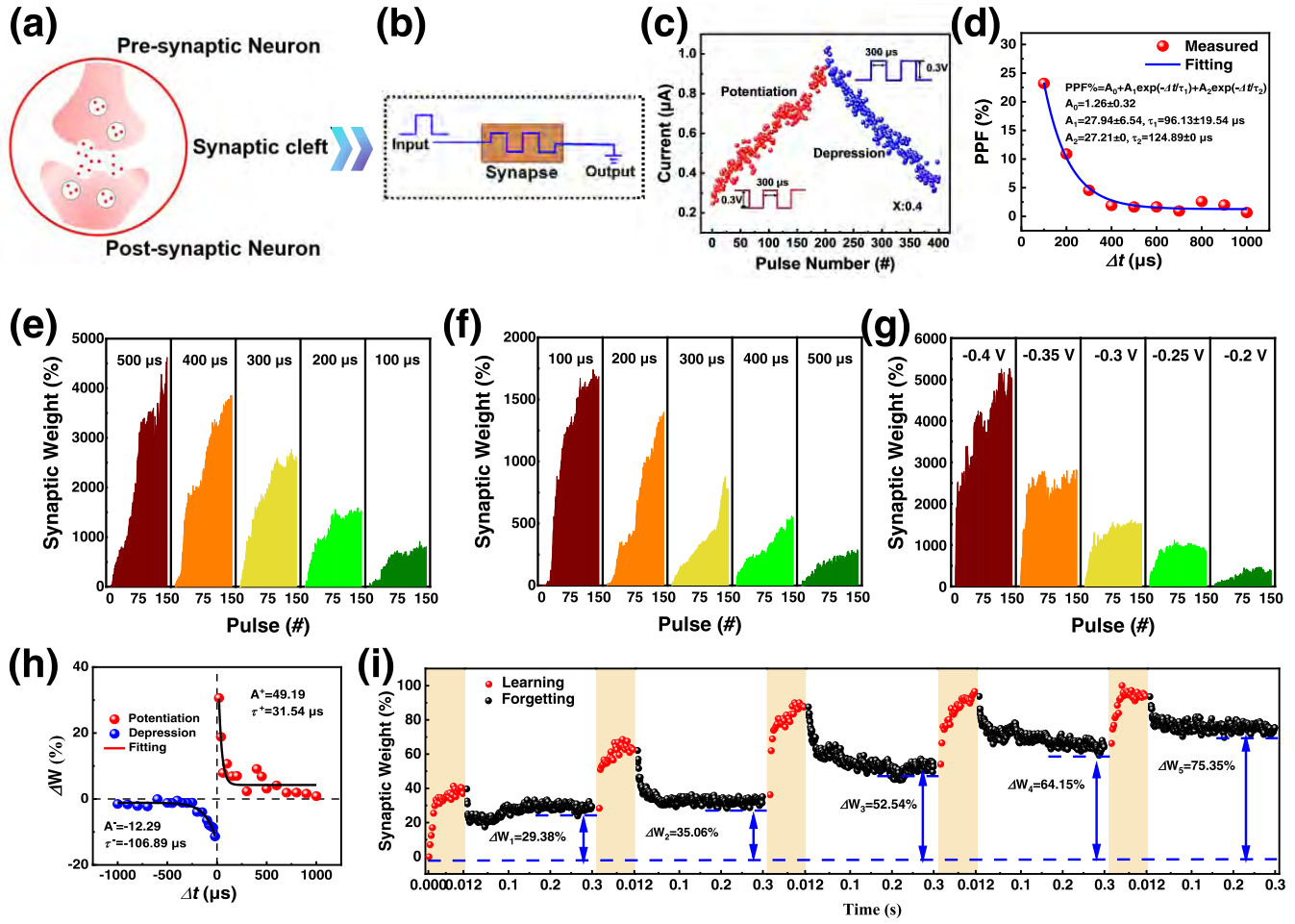

Figure 5. (a) Schematic diagram of the biological synapse, (b) full memristor-based artificial circuit, (c) potentiation and depression by consecutive pulses, and (d) PPF behavior of the device. Synaptic plasticity by modulation (e) width (−0.3 V, 200 μs interval), (f) interval (−0.3 V, 200 μs width), and (g) amplitude (200 μs width and 200 μs interval). (h) STDP behavior of the device. (i) "Learning−forgetting−relearning" process for five cycles.

exponential decay function corresponding to the device is given by[45]

$$\mathrm{PPF}\% = A_0 + A_1 \exp(-\Delta t/\tau_1) + A_2 \exp(-\Delta t/\tau_2) \quad (2)$$

where A_0 is the constant of 1.26 ± 0.32, A_1 and A_2 are the initial facilitation magnitudes of the first and second responses of 27.94 ± 6.54 and 27.21 ± 0, respectively, and Δt is the time interval between the pair of stimuli. The characteristic relaxation times τ_1 and τ_2 of the first and second responses are 96.13 ± 19.54 and 124.89 ± 0 μs, respectively. Energy efficiency is also important to artificial synapses in practical applications. In our device, a voltage pulse of −0.3 V with a width of 200 μs triggers an EPSC of 1.17 μA (Figure S9), and the energy consumption is calculated at ∼70 pJ. The performance indicators are compared statistically with those in the literature, as shown in Figure S10 and Table S3.

Stimuli from the external environment affect the neural activity of the biological brain. Here, synaptic plasticity is simulated by applying pulse stimuli with different pulse widths (100, 200, 300, 400, and 500 μs), pulse intervals (100, 200, 300, 400, and 500 μs), and pulse amplitudes (−0.2, −0.25, −0.3, −0.35, and −0.4 V), as shown in Figure 5e−g, respectively. By applying different pulse widths at a fixed pulse amplitude of −0.3 V and a pulse interval of 200 μs as shown in Figure 5e, the larger the pulse width, the greater is the synaptic weight change. Similarly, by changing the pulse interval at a fixed pulse amplitude of −0.3 V and a pulse width of 200 μs, it is found that the smaller the pulse interval, the greater is the synaptic weight change, as shown in Figure 5f. When the pulse amplitude is changed from −0.2 to −0.4 V, the synaptic weight is increased for the same fixed pulse width and pulse interval (200 μs, 200 μs), as shown in Figure 5g. The change in the synaptic weight is described by the following equation[46]

$$W\% = [(G_n - G_0)/G_0] \times 100\% \quad (3)$$

where G_0 is the conductance in the initial state and G_n (n = 1,2,3, ···150) is the corresponding conductance after stimulation.

Spike-timing-dependent plasticity (STDP) plays an important role in human learning and memory and is expressed as follows[21]

$$\Delta W = \begin{cases} A_+ \exp\left(\dfrac{\Delta t}{\tau_+}\right) + W_0, \ \Delta t > 0 \\ A_- \exp\left(\dfrac{\Delta t}{\tau_-}\right) + W_0, \ \Delta t < 0 \end{cases} \quad (4)$$

https://doi.org/10.1021/acsanm.3c01203
ACS Appl. Nano Mater. 2023, 6, 7975−7983

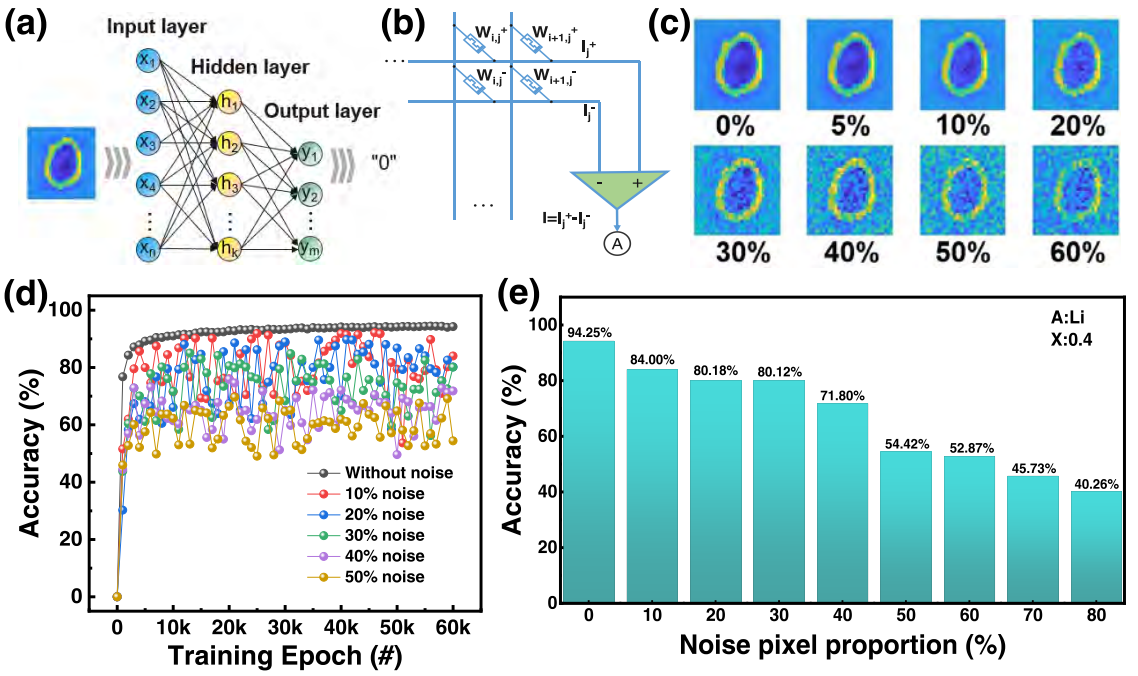

Figure 6. (a) Schematic of the three-layer neural network for recognition of handwritten digits. (b) Schematic of the synaptic weight defined as the conductance difference of two equivalent synapses. (c) Synaptic weight mapping images after training of digits "0" with different noise ratios (0–60%) in the neural network. (d, e) Recognition accuracy of the network in the flat state as a function of the training epochs and noise pixel.

where A and τ are the scale factor and time constant, respectively, and W_0 is the constant representing unassociated synaptic regulation. The prespike is sent to the Ag electrode and the postspike is sent to the ITO electrode. When the presynaptic pulse is triggered before the postsynaptic pulse ($\Delta t > 0$), the device undergoes the LTP, showing a more pronounced increase in ΔW as Δt decreases. Conversely, LTD occurs when the presynaptic pulse arrives after the postsynaptic pulse ($\Delta t < 0$). Here, τ_+ and τ_- are 31.54 μs and −106.89 μs in the antisymmetric Hebbian learning rules, respectively, which match the time constants in biological synapses as shown in Figure 5h. The repetitive learning behavior is assessed by applying the same continuous voltage pulse after a certain time interval. Five learning–forgetting processes are implemented as shown in Figure 5i. The 30 consecutive negative voltage pulses (−0.3 V, 200 μs) are applied to the device and the voltage pulses are turned off for 0.3 s. The synaptic weight changes are 29.38, 35.06, 52.54, 64.15, and 75.35%, similar to how humans reinforce memories through repetitive learning. In the process of forgetting, spontaneous diffusion of V_I due to joule heat leads to rapid decay of the synaptic weight,[47] known as short-term plasticity (STP). The adsorption function based on the pores in the volcanic structure slows the diffusion of ions, leading to the slow decline of the synaptic weight with increasing forgetting time, which is known as long-term plasticity (LTP). The phenomenon is similar to the process of forgetting in the human brain.

In order to explore the application to NC, a handwritten artificial neural network (ANN) is developed to simulate learning digits from the Modified National Institute of Standards and Technology (MNIST) dataset through a backpropagation (BP) neural network simulator shown in Figure 6. The simulator can recognize an image utilizing 28 × 28 input neurons and 100 hidden neurons, and the 10 output neurons correspond to 10 classes of digits (0–9) as illustrated in Figure 6a. Figure 6b reveals that a signed weight is mapped to the differential conductance of a pair of memristors. We consider the change in the conductivity of the input neurons due to the input voltage signal as the synaptic weight ($W = G^+ - G^-$) and obtain the processed output neuron current by matrix multiplication of the input signal. In order to study the influence of device stability on the network performance, different levels of noise (0–60%) are applied to the device and image, respectively. In order to reflect the degree of noise more directly, Figure 6c shows the change of the picture clarity with noise. The potentiation/depression data in Figure 5c is defined as the synaptic weight update to implement pattern recognition and add Gaussian noise to the fitting data to obtain the pulse response of the simulator. A device pulse response model with Gaussian noise is used to simulate the fluctuation of the resistance state of the test data. Figure 6d,e shows the variation of the recognition accuracy with time between training iterations and noise ratios, respectively. The accuracy can reach 94.25% without noise. When the noise ratio is 60%, the recognition accuracy is still higher than 50%, demonstrating a strong fault tolerance capability.

CONCLUSIONS

A biomimetic synaptic device doped with lithium shows a set voltage as low as −0.1 V and a retention time of 10^4 s. The multilevel storage characteristics and artificial synaptic properties are simulated. The underlying mechanism of the device is analyzed and discussed inspired by natural volcanic rocks. The synaptic device with stable memristive characteristics can be applied to image recognition with an accuracy rate of 94.25%, and the strategy and results provide insights into the development of future neuromorphic computing systems.

https://doi.org/10.1021/acsanm.3c01203
ACS Appl. Nano Mater. 2023, 6, 7975–7983

■ ASSOCIATED CONTENT

Supporting Information

The Supporting Information is available free of charge at https://pubs.acs.org/doi/10.1021/acsanm.3c01203.

Computational methods; cross-sectional characterization of Ag/$CBL_{0.4}I$/ITO; particle size analysis of CBL_xI (x = 0, 0.2, 0.4, 0.6) perovskite films; AFM images of CBL_xI (x = 0, 0.2, 0.4, 0.6) perovskite films; electrical characteristics of Ag/CBL_xI (x = 0, 0.2, 0.4, 0.6)/ITO devices; conduction mechanism analysis of Ag/$CBL_{0.4}I$/ITO; parameter summary of lead-free perovskite-based memristors; cumulative memory effects of Ag/$CBL_{0.4}I$/ITO; EPSC behavior of Ag/$CBL_{0.4}I$/ITO; and summary of energy consumption parameters for perovskite-based synaptic memristors (PDF)

■ AUTHOR INFORMATION

Corresponding Authors

Qin Gao − *School of Physics & School of Chemistry, Beihang University, Beijing 100191, China;* orcid.org/0000-0002-0573-9774; Email: gaoqin@buaa.edu.cn

Anping Huang − *School of Physics, Beihang University, Beijing 100191, China;* orcid.org/0000-0002-1365-3575; Email: aphuang@buaa.edu.cn

Authors

Juan Gao − *School of Physics, Beihang University, Beijing 100191, China*

Jiangshun Huang − *School of Physics, Beihang University, Beijing 100191, China*

Xiaoyue Feng − *School of Physics, Beihang University, Beijing 100191, China*

Xueli Geng − *School of Physics, Beihang University, Beijing 100191, China*

Haoze Li − *School of Physics, Beihang University, Beijing 100191, China*

Guoxing Wang − *School of Physics, Beihang University, Beijing 100191, China*

Bo Liang − *School of Physics, Beihang University, Beijing 100191, China*

Xueliang Chen − *School of Physics, Beihang University, Beijing 100191, China*

Yuanzhao Su − *School of Aeronautic Science and Engineering, Beihang University, Beijing 100191, China*

Mei Wang − *School of Physics, Beihang University, Beijing 100191, China*

Zhisong Xiao − *School of Physics, Beihang University, Beijing 100191, China;* orcid.org/0000-0001-7309-9900

Paul K. Chu − *Department of Physics, Department of Materials Science and Engineering, and Department of Biomedical Engineering, City University of Hong Kong, Hong Kong, China;* orcid.org/0000-0002-5581-4883

Complete contact information is available at: https://pubs.acs.org/10.1021/acsanm.3c01203

Notes

The authors declare no competing financial interest.

■ ACKNOWLEDGMENTS

This research was supported by the National Natural Science Foundation of China (Grant Nos. 51872010 and 61975005), Foundation of Beijing Academy of Quantum Information Sciences (Grant No. Y18G28), and City University of Hong Kong Donation Research Grant (DON-RMG No. 9229021).

■ REFERENCES

(1) Yang, J.-Q.; Wang, R.; Wang, Z.-P.; Ma, Q.-Y.; Mao, J.-Y.; Ren, Y.; Yang, X.; Zhou, Y.; Han, S.-T. Leaky integrate-and-fire neurons based on perovskite memristor for spiking neural networks. *Nano Energy* **2020**, *74*, No. 104828.

(2) John, R. A.; Yantara, N.; Ng, S. E.; Patdillah, M. I. B.; Kulkarni, M. R.; Jamaludin, N. F.; Basu, J.; Ankit; Mhaisalkar, S. G.; Basu, A.; Mathews, N. Diffusive and Drift Halide Perovskite Memristive Barristors as Nociceptive and Synaptic Emulators for Neuromorphic Computing. *Adv. Mater.* **2021**, *33*, No. 2007851.

(3) Hao, J.; Kim, Y.-H.; Habisreutinger, S. N.; Harvey, S. P.; Miller, E. M.; Foradori, S. M.; Arnold, M. S.; Song, Z.; Yan, Y.; Luther, J. M.; Blackburn, J. L. Low-energy room-temperature optical switching in mixed-dimensionality nanoscale perovskite heterojunctions. *Sci. Adv.* **2021**, *7*, No. eabf1959.

(4) Gong, J.; Wei, H.; Liu, J.; Sun, L.; Xu, Z.; Huang, H.; Xu, W. An artificial visual nerve for mimicking pupil reflex. *Matter* **2022**, *5*, 1578−1589.

(5) John, R. A.; Demirag, Y.; Shynkarenko, Y.; Berezovska, Y.; Ohannessian, N.; Payvand, M.; Zeng, P.; Bodnarchuk, M. I.; Krumeich, F.; Kara, G.; Shorubalko, I.; Nair, M. V.; Cooke, G. A.; Lippert, T.; Indiveri, G.; Kovalenko, M. V. Reconfigurable halide perovskite nanocrystal memristors for neuromorphic computing. *Nat. Commun.* **2022**, *13*, No. 2074.

(6) Yoo, E. J.; Lyu, M.; Yun, J. H.; Kang, C. J.; Choi, Y. J.; Wang, L. Resistive Switching Behavior in Organic-Inorganic Hybrid $CH_3NH_3PbI_{3-x}Cl_x$ Perovskite for Resistive Random Access Memory Devices. *Adv. Mater.* **2015**, *27*, 6170−6175.

(7) Xu, W.; Cho, H.; Kim, Y. H.; Kim, Y. T.; Wolf, C.; Park, C. G.; Lee, T. W. Organometal Halide Perovskite Artificial Synapses. *Adv. Mater.* **2016**, *28*, 5916−5922.

(8) Zhu, X.; Lu, W. D. Optogenetics-Inspired Tunable Synaptic Functions in Memristors. *ACS Nano* **2018**, *12*, 1242−1249.

(9) Ham, S.; Choi, S.; Cho, H.; Na, S.-I.; Wang, G. Photonic Organolead Halide Perovskite Artificial Synapse Capable of Accelerated Learning at Low Power Inspired by Dopamine-Facilitated Synaptic Activity. *Adv. Funct. Mater.* **2019**, *29*, No. 1806646.

(10) Zhao, X.; Xu, H.; Wang, Z.; Lin, Y.; Liu, Y. Memristors with organic-inorganic halide perovskites. *InfoMat* **2019**, *1*, 183−210.

(11) Poddar, S.; Zhang, Y.; Gu, L.; Zhang, D.; Zhang, Q.; Yan, S.; Kam, M.; Zhang, S.; Song, Z.; Hu, W.; Liao, L.; Fan, Z. Down-Scalable and Ultra-fast Memristors with Ultra-high Density Three-Dimensional Arrays of Perovskite Quantum Wires. *Nano Lett.* **2021**, *21*, 5036−5044.

(12) Zhang, J.; Sun, T.; Zeng, S.; Hao, D.; Yang, B.; Dai, S.; Liu, D.; Xiong, L.; Zhao, C.; Huang, J. Tailoring neuroplasticity in flexible perovskite QDs-based optoelectronic synaptic transistors by dual modes modulation. *Nano Energy* **2022**, *95*, No. 106987.

(13) Cheng, X.-F.; Qian, W.-H.; Wang, J.; Yu, C.; He, J.-H.; Li, H.; Xu, Q.-F.; Chen, D.-Y.; Li, N.-J.; Lu, J.-M. Environmentally Robust Memristor Enabled by Lead-Free Double Perovskite for High-Performance Information Storage. *Small* **2019**, *15*, No. 1905731.

(14) Xiao, X.; Hu, J.; Tang, S.; Yan, K.; Gao, B.; Chen, H.; Zou, D. Recent Advances in Halide Perovskite Memristors: Materials, Structures, Mechanisms, and Applications. *Adv. Mater. Technol.* **2020**, *5*, No. 1900914.

(15) Zeng, F.; Guo, Y.; Hu, W.; Tan, Y.; Zhang, X.; Feng, J.; Tang, X. Opportunity of the Lead-Free All-Inorganic $Cs_3Cu_2I_5$ Perovskite Film for Memristor and Neuromorphic Computing Applications. *ACS Appl. Mater. Interfaces* **2020**, *12*, 23094−23101.

(16) Kim, S.-Y.; Park, D.-A.; Park, N.-G. Synthetic Powder-Based Thin (<0.1 μm) Cs3Bi2Br9 Perovskite Films for Air-Stable and Viable Resistive Switching Memory. *ACS Appl. Electron. Mater.* **2022**, *4*, 2388−2395.

(17) Hu, Y.; Zhang, S.; Miao, X.; Su, L.; Bai, F.; Qiu, T.; Liu, J.; Yuan, G. Ultrathin $Cs_3Bi_2I_9$ Nanosheets as an Electronic Memory

Material for Flexible Memristors. *Adv. Mater. Interfaces* **2017**, *4*, No. 1700131.
(18) Xiong, Z.; Hu, W.; She, Y.; Lin, Q.; Hu, L.; Tang, X.; Sun, K. Air-Stable Lead-Free Perovskite Thin Film Based on $CsBi_3I_{10}$ and Its Application in Resistive Switching Devices. *ACS Appl. Mater. Interfaces* **2019**, *11*, 30037−30044.
(19) Ge, S.; Guan, X.; Wang, Y.; Lin, C.-H.; Cui, Y.; Huang, Y.; Zhang, X.; Zhang, R.; Yang, X.; Wu, T. Low-Dimensional Lead-Free Inorganic Perovskites for Resistive Switching with Ultralow Bias. *Adv. Funct. Mater.* **2020**, *30*, No. 2002110.
(20) Kwak, K. J.; Baek, J. H.; Lee, D. E.; Im, I. H.; Kim, J.; Kim, S. J.; Lee, Y. J.; Kim, J. Y.; Jang, H. W. Ambient Stable All Inorganic $CsCu_2I_3$ Artificial Synapses for Neurocomputing. *Nano Lett.* **2022**, *22*, 6010−6017.
(21) Lao, J.; Xu, W.; Jiang, C.; Zhong, N.; Tian, B.; Lin, H.; Luo, C.; Travas-sejdic, J.; Peng, H.; Duan, C.-G. An air-stable artificial synapse based on a lead-free double perovskite $Cs_2AgBiBr_6$ film for neuromorphic computing. *J. Mater. Chem. C* **2021**, *9*, 5706−5712.
(22) Hwang, B.; Lee, J.-S. Lead-free, air-stable hybrid organic−inorganic perovskite resistive switching memory with ultrafast switching and multilevel data storage. *Nanoscale* **2018**, *10*, 8578−8584.
(23) He, N.; Ye, F.; Liu, J.; Sun, T.; Wang, X.; Hou, W.; Shao, W.; Wan, X.; Tong, Y.; Xu, F.; Sheng, Y. Multifunctional Ag−In−Zn−S/$Cs_3Cu_2I_5$-Based Memristors with Coexistence of Non-Volatile Memory and Volatile Threshold Switching Behaviors for Neuro-inspired Computing. *Adv. Electron. Mater.* **2022**, *9*, No. 2201038.
(24) Lyu, C.; Liu, C.; Min, H.; Shi, X.; Jiang, R.; Ao, Z.; Zhang, X.; Wang, C.; Ma, H.; Wang, L. Rare earth Nd-doping lead-free double perovskite $Cs_2AgBiBr_6$ films with improved resistive memory performance. *J. Alloys Compd.* **2022**, *913*, No. 165300.
(25) Paramanik, S.; Maiti, A.; Chatterjee, S.; Pal, A. J. Large Resistive Switching and Artificial Synaptic Behaviors in Layered $Cs_3Sb_2I_9$ Lead-Free Perovskite Memory Devices. *Adv. Electron. Mater.* **2022**, *8*, No. 2100237.
(26) Kim, S. G.; Van Le, Q.; Han, J. S.; Kim, H.; Choi, M.-J.; Lee, S. A.; Kim, T. L.; Kim, S. B.; Kim, S. Y.; Jang, H. W. Dual-Phase All-Inorganic Cesium Halide Perovskites for Conducting-Bridge Memory-Based Artificial Synapses. *Adv. Funct. Mater.* **2019**, *29*, No. 1906686.
(27) Zhou, Y.; Chen, J.; Bakr, O. M.; Sun, H.-T. Metal-Doped Lead Halide Perovskites: Synthesis, Properties, and Optoelectronic Applications. *Chem. Mater.* **2018**, *30*, 6589−6613.
(28) Gao, Q.; Huang, A.; Hu, Q.; Zhang, X.; Chi, Y.; Li, R.; Ji, Y.; Chen, X.; Zhao, R.; Wang, M.; Shi, H.; Wang, M.; Cui, Y.; Xiao, Z.; Chu, P. K. Stability and Repeatability of a Karst-like Hierarchical Porous Silicon Oxide-Based Memristor. *ACS Appl. Mater. Interfaces* **2019**, *11*, 21734−21740.
(29) Snega, S.; Ravichandran, K.; Baneto, M.; Vijayakumar, S. Simultaneous Enhancement of Transparent and Antibacterial Properties of ZnO Films by Suitable F Doping. *J. Mater. Sci. Technol.* **2015**, *31*, 759−765.
(30) Balakarthikeyan, R.; Santhanam, A.; Anandhi, R.; Vinoth, S.; Al-Baradi, A. M.; Alrowaili, Z. A.; Al-Buriahi, M. S.; Deva Arun Kumar, K. Fabrication of nanostructured NiO and NiO:Cu thin films for high-performance ultraviolet photodetector. *Opt. Mater.* **2021**, *120*, No. 111387.
(31) Ibrahem, I.; Zhao, G.-L.; Córdova, A. Direct Catalytic Enantioselective α-Aminomethylation of Aldehydes. *Chem. − Eur. J.* **2007**, *13*, 683−688.
(32) Yao, H.; Zhou, F.; Li, Z.; Ci, Z.; Ding, L.; Jin, Z. Strategies for Improving the Stability of Tin-Based Perovskite ($ASnX_3$) Solar Cells. *Adv. Sci.* **2020**, *7*, No. 1903540.
(33) Hussain, A. A. Constructing Caesium-Based Lead-Free Perovskite Photodetector Enabling Self-Powered Operation with Extended Spectral Response. *ACS Appl. Mater. Interfaces* **2020**, *12*, 46317−46329.
(34) Xiao, Z.; Huang, J. Energy-Efficient Hybrid Perovskite Memristors and Synaptic Devices. *Adv. Electron. Mater.* **2016**, *2*, No. 1600100.
(35) Shao, Y.; Fang, Y.; Li, T.; Wang, Q.; Dong, Q.; Deng, Y.; Yuan, Y.; Wei, H.; Wang, M.; Gruverman, A.; Shield, J.; Huang, J. Grain boundary dominated ion migration in polycrystalline organic−inorganic halide perovskite films. *Energy Environ. Sci.* **2016**, *9*, 1752−1759.
(36) Kim, S. J.; Lee, T. H.; Yang, J.-M.; Yang, J. W.; Lee, Y. J.; Choi, M.-J.; Lee, S. A.; Suh, J. M.; Kwak, K. J.; Baek, J. H.; Im, I. H.; Lee, D. E.; Kim, J. Y.; Kim, J.; Han, J. S.; Kim, S. Y.; Lee, D.; Park, N.-G.; Jang, H. W. Vertically aligned two-dimensional halide perovskites for reliably operable artificial synapses. *Mater. Today* **2022**, *52*, 19−30.
(37) Sun, Y.; Tai, M.; Song, C.; Wang, Z.; Yin, J.; Li, F.; Wu, H.; Zeng, F.; Lin, H.; Pan, F. Competition between Metallic and Vacancy Defect Conductive Filaments in a $CH_3NH_3PbI_3$-Based Memory Device. *J. Phys. Chem. C* **2018**, *122*, 6431−6436.
(38) Li, D.; Dong, X.; Cheng, P.; Song, L.; Wu, Z.; Chen, Y.; Huang, W. Metal Halide Perovskite/Electrode Contacts in Charge-Transporting-Layer-Free Devices. *Adv. Sci.* **2022**, *9*, No. 2203683.
(39) Gonzales, C.; Guerrero, A. Mechanistic and Kinetic Analysis of Perovskite Memristors with Buffer Layers: The Case of a Two-Step Set Process. *J. Phys. Chem. Lett.* **2023**, *14*, 1395−1402.
(40) Wang, G.; Lee, J.-H.; Yang, Y.; Ruan, G.; Kim, N. D.; Ji, Y.; Tour, J. M. Three-Dimensional Networked Nanoporous Ta_2O_{5-x} Memory System for Ultrahigh Density Storage. *Nano Lett.* **2015**, *15*, 6009−6014.
(41) Ontiveros-Ortega, A.; Vidal, F.; Gimenez, E.; Ibáñez, J. M. Effect of heavy metals on the surface free energy and zeta potential of volcanic glass: implications on the adhesion and growth of microorganisms. *J. Mater. Sci. Technol.* **2014**, *49*, 3550−3559.
(42) Liu, Z.; Cheng, P.; Kang, R.; Zhou, J.; Zhao, X.; Zhao, J.; Zuo, Z. Photo-Enhanced Resistive Switching Effect in High-Performance $MAPbI_3$ Memristors. *Adv. Mater. Interfaces* **2023**, *10*, No. 2201513.
(43) Liu, Z.; Tang, H.; Cheng, P.; Kang, R.; Zhou, J.; Zhao, X.; Zhao, J.; Zuo, Z. High-Performance and Environmentally Robust Multilevel Lead-Free Organotin Halide Perovskite Memristors. *Adv. Electron. Mater.* **2022**, *9*, No. 2201005.
(44) Wang, K.; Chen, J.; Yan, X. MXene Ti_3C_2 memristor for neuromorphic behavior and decimal arithmetic operation applications. *Nano Energy* **2021**, *79*, No. 105453.
(45) Gao, Q.; Huang, J.; Gao, J.; Geng, X.; Ji, Y.; Li, H.; Wang, G.; Liang, B.; Wang, M.; Xiao, Z.; Zhu, Y.; Chu, P. K.; Huang, A. Tunable plasticity in functionalized honeycomb synaptic memristor for neurocomputing. *Mater. Today Phys.* **2023**, *30*, No. 100947.
(46) Shan, X.; Zhao, C.; Wang, X.; Wang, Z.; Fu, S.; Lin, Y.; Zeng, T.; Zhao, X.; Xu, H.; Zhang, X.; Liu, Y. Plasmonic Optoelectronic Memristor Enabling Fully Light-Modulated Synaptic Plasticity for Neuromorphic Vision. *Adv. Sci.* **2022**, *9*, No. 2104632.
(47) Mao, J.-Y.; Zheng, Z.; Xiong, Z.-Y.; Huang, P.; Ding, G.-L.; Wang, R.; Wang, Z.-P.; Yang, J.-Q.; Zhou, Y.; Zhai, T.; Han, S.-T. Lead-free monocrystalline perovskite resistive switching device for temporal information processing. *Nano Energy* **2020**, *71*, No. 104616.

https://doi.org/10.1021/acsanm.3c01203
ACS Appl. Nano Mater. 2023, 6, 7975−7983

Supporting Information

Influence of Lithium Doping on Volcanic-like Perovskite Memristors and Artificial Synaptic Simulation for Neurocomputing

*Juan Gao [1], Qin Gao *[,2], Jiangshun Huang [1], Xiaoyue Feng [1], Xueli Geng [1], Haoze Li [1], Guoxing Wang [1], Bo Liang [1], Xueliang Chen [1], Yuanzhao Su [3], Mei Wang [1], Zhisong Xiao [1], Paul K. Chu [4], Anping Huang [*,1]*

[1] School of Physics, Beihang University, Beijing 100191, China

[2] School of Physics & School of Chemistry, Beihang University, Beijing 100191, China

[3] School of Aeronautic Science and Engineering, Beihang University, Beijing 100191, China

[4] Department of Physics, Department of Materials Science and Engineering, and Department of Biomedical Engineering, City University of Hong Kong, Tat Chee Avenue, Kowloon, Hong Kong, China

** Corresponding Authors*

Qin Gao − Email: gaoqin@buaa.edu.cn (Dr. Qin Gao)

Anping Huang − Email: aphuang@buaa.edu.cn (Dr. A. P. Huang)

Table of contents

1. Computational Methods

The Vienna *ab initio* simulation package (VASP) with the projector-augmented-wave pseudopotential is used in the first-principles calculation.[1-3] The Perdew-Burke-Ernzerhof (PBE) functional based on the generalized gradient approximation (GGA) is implemented for the electronic exchange correlation functional.[4] Although the density-functional theory (DFT) calculation underestimates the bandgap, the tendency of the defect formation energy is almost unaffected by the functional and the hybrid functional method[5] is very expensive. Therefore, the DFT method is adopted in this work. The cutoff energy of the plane wave basis is set to 400 eV in the calculation. A 5×5×3 Monkhorst-Pack grid[6] is used for *k*-point sampling of the CBI primitive cell. The optimized lattice parameters a and c were 8.39 Å and 21.20 Å, respectively. A single k-point was sampled in the overall defective calculation and all the geometries are fully relaxed with the Hellman-Feynman force of each atom converging below 0.01 eV/Å. The defect formation energy is calculated by the following equation:

$$E_f = E_D - E_0 - \sum_i n_i \mu_i \qquad (1)$$

where E_D and E_0 are the energy of system with and without defects, respectively, μ_i represents the single-atom chemical potential used to show the effects of adding ($n_i < 0$) or removing ($n_i > 0$) atoms to/from the system on the energy of the structure.

Table S1. NaBi", KBi" and LiBi" represents Bi replaced by Na, K, and Li respectively, and LiCs" represents Cs replaced by Li element. V_I- LiBi" and V_I- LiCs" are the abbreviated forms of complex defects representing Bi/Cs replaced by Li and leaving an iodine vacancy (V_I), respectively. The defect formation energy (DFE) of Bi replaced by Li is 0.66 eV and lower than Na and K substitution of 0.70 eV and 0.92 eV, respectively. The DFE of Cs replaced by Li is 1.46 eV, indicating that Li can replace Bi easily as shown in Table S1. The DFE of V_I produced by Li replacing Bi (3.67 eV) is lower than that produced by Li replacing Cs (5.89 eV), indicating that Li replacement of Bi is easier in producing the V_I.

Table S1. Formation energy of different defect types

Defect Type	NaBi"	KBi"	LiBi"	LiCs"	V_I- LiBi"	V_I- LiCs"
DFE (eV)	0.70	0.92	0.66	1.46	3.67	5.89

2. Cross-sectional characterization of Ag/$CBL_{0.4}I$/ITO

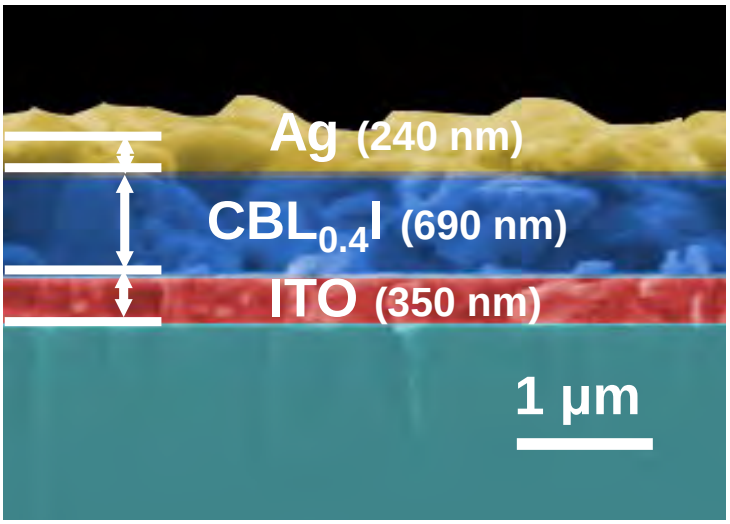

Figure S1. Cross-sectional SEM images of $CBL_{0.4}I$-based memristor.

3. Particle size analysis of CBL_xI (x=0, 0.2, 0.4, 0.6) perovskite films

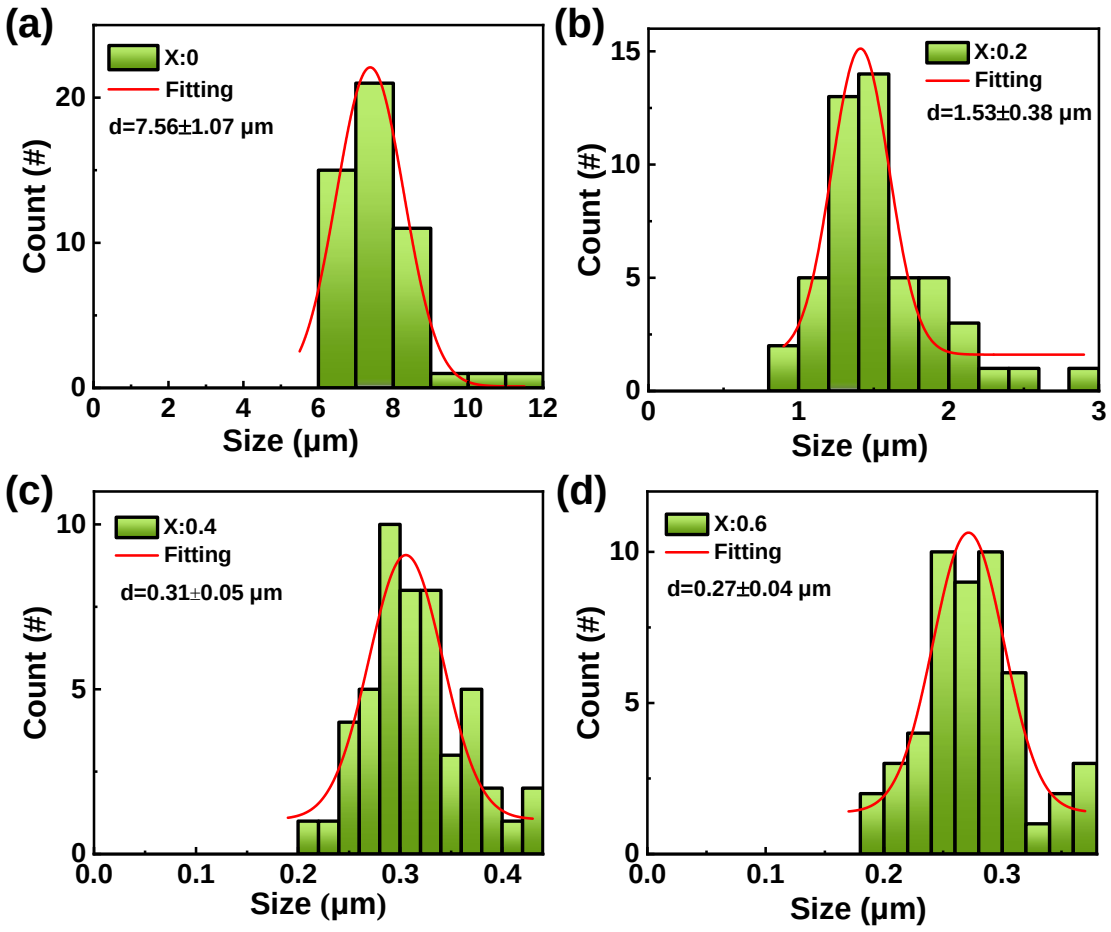

Figure S2. The Nano-Measure Particle Size Statistics software is used to calculate the grain size of the perovskite films with different doping concentrations. Statistical grain size distributions of the device (a) x = 0; (b) x = 0.2; (c) x = 0.4; and (d) x = 0.6. The average grain size is ~ 7.56 μm, ~ 1.53 μm, ~ 0.31 μm and ~ 0.27 μm, respectively.

4. AFM images of CBL_xI (x=0, 0.2, 0.4, 0.6) perovskite films

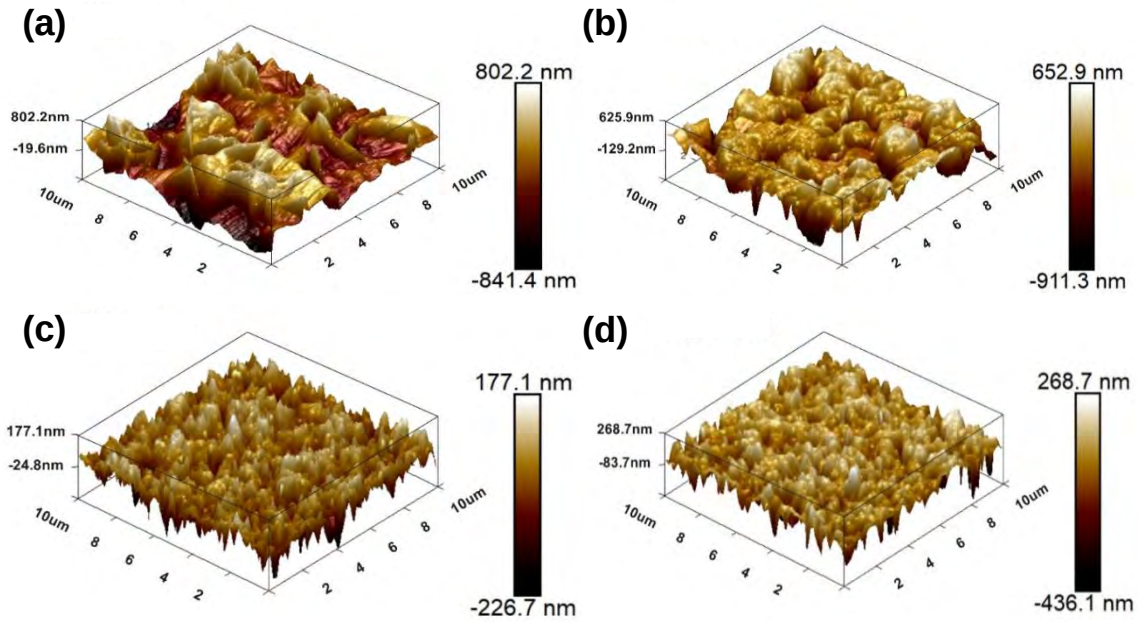

Figure S3. AFM images of the CBL_xI (a) x=0; (b) x=0.2; (c) x=0.4; (d) x=0.6. The root-mean-square roughness is ~ 307 nm, ~ 231 nm, ~ 56 nm and ~ 91 nm, respectively.

5. Electrical characteristics of Ag/CBL$_x$I (x=0, 0.2, 0.4, 0.6)/ITO devices

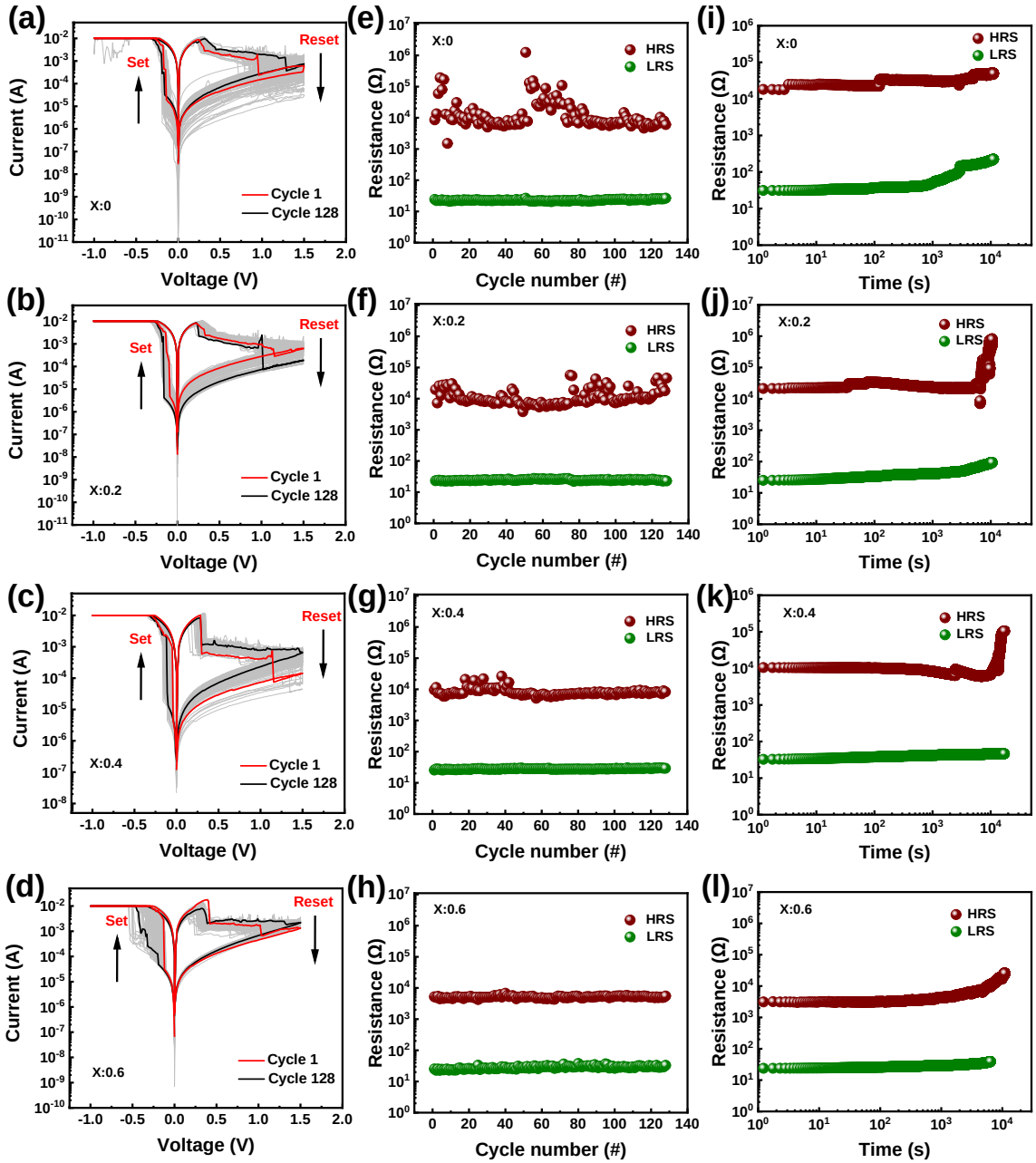

Figure S4. (a)-(d) *I-V* curves of the perovskite films with different Li doping concentrations; (e)-(h) Endurance of the perovskite films with different Li doping concentrations; (i)-(l) Retention of the perovskite films with different Li doping concentrations.

6. Conduction mechanism analysis of $Ag/CBL_{0.4}I/ITO$

To investigate the conduction mechanism in CBL_xI-based perovskite memristors, log (I)-log (V) curve is illustrated in Figure S5. In set process [Figure S5(a)], the HRS progress with a slope (S1) of 1.06, corresponding to the ohmic conduction,[7,8] which means that the number of thermally excited carriers are more than the number of injected carriers. As the voltage increase, the traps within the perovskite layer begin to fill, and when all the traps are filled, the current jumps sharply, conforming to the trap-filled limited region (TFL region).[9] With increasing voltage, the fitted slope of HRS about 2.69, it means that transport behavior obeys the relation of I-V^2, the traps would be filled gradually, agreeing with the SCLC model.[10] After the SCLC region, the state of the device switch to the LRS, the slope is about 1.0, and the corresponding conduction mechanism obeys ohmic conduction. Both the ohmic conduction behavior in the LRS and sharp current increases in the set process are typical features of the conductive filament(CF) mode in the resistive switching mechanism.[11] In the initial state, V_I is randomly distributed in the perovskite layer. When negative bias is applied to the Ag electrode, the V_I migrates to the Ag and accumulates, then CF grows to the ITO and finally forms a complete CF connecting the top and bottom electrodes. At this time, the electronic channel is opened and the device switches to LRS. In reset process [Figure S5(b)], when the opposite voltage is applied to the memristor, the conduction mechanism changed from ohmic (Slope1: 1.02) to SCLC (Slope2: 1.80), which mean that the trapped electrons are extracted with the increase of the positive voltage.[9] This process is accompanied by the gradual breaking of the CF generated

by the combination of V_I and I^-. Subsequently, the device is switched to HRS, obeying SCLC and ohmic conduction mechanism.

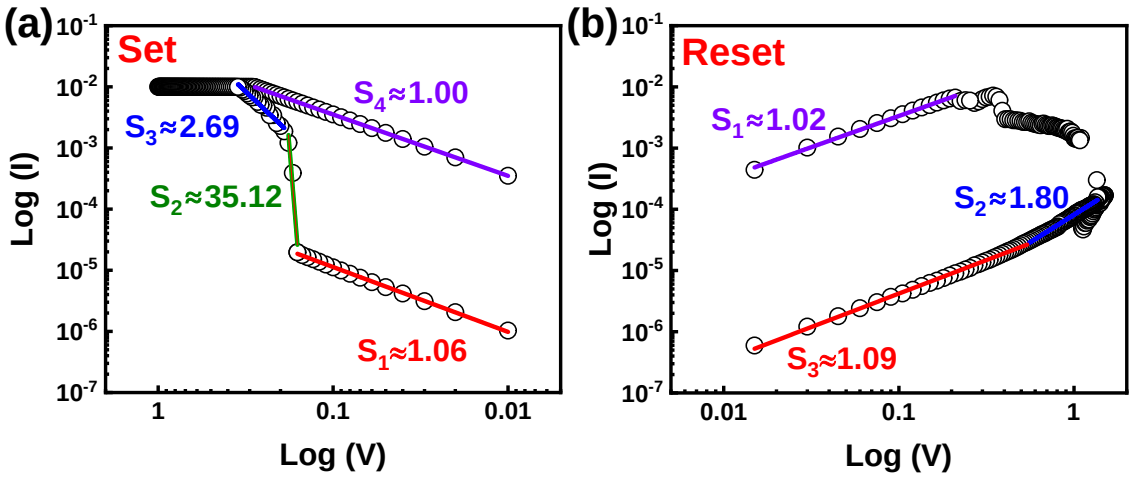

Figure S5. *I–V* curve in log–log scale in the (a) positive voltage sweeping region and (b) negative voltage sweeping region.

To further demonstrate that resistance behavior is mainly caused by the formation and fracture of the V_I CF, the influence of different electrode areas, electrodes materials, such as Pt, Au Ag and Cu were applied to analyze the resistive behavior of the device as shown in Figure S6. As shown in Figure S6(a), the LRS distribution of the memristors is almost area-independent and agreed well with the CF-based conduction mechanism. The mechanism of CF has been reported in the study of halide perovskite based memristor. In this work, V_I has a lower activation energy (0.32 eV)[12] than other components in perovskite films, and Ag is an active metal prone to electrochemical metallization. The conductive mechanism may come from V_I CF and Ag CF. In order to further explore the mechanism, different top electrodes (Pt, Au, Ag, Cu) are used to prepare the devices, the *I-V* characteristic curves shown in Figure S6(b-e), respectively, the devices all exhibit similar resistance switching behavior. It is worth noting that the set voltage of with the active electrode (Ag, Cu) is smaller than that of the inert electrode (Pt, Au), as shown in Figure S6(f), mainly because the active electrode Ag (Cu) reacts with the I^- in the perovskite layer to form AgI (CuI), which creates more V_I, facilitates the formation of CF and reduces the set voltage, consistent with previously reports.[12] In addition, in our work, the set process occurs during the negative voltage sweep on the Ag electrode, the reverse driving force limited the movement of Ag^+, but is conducive to the accumulation and formation of V_I CF. It should be pointed out that the resistive switching mechanism in this work is dominated by the formation and fracture of V_I CF. [12-15]

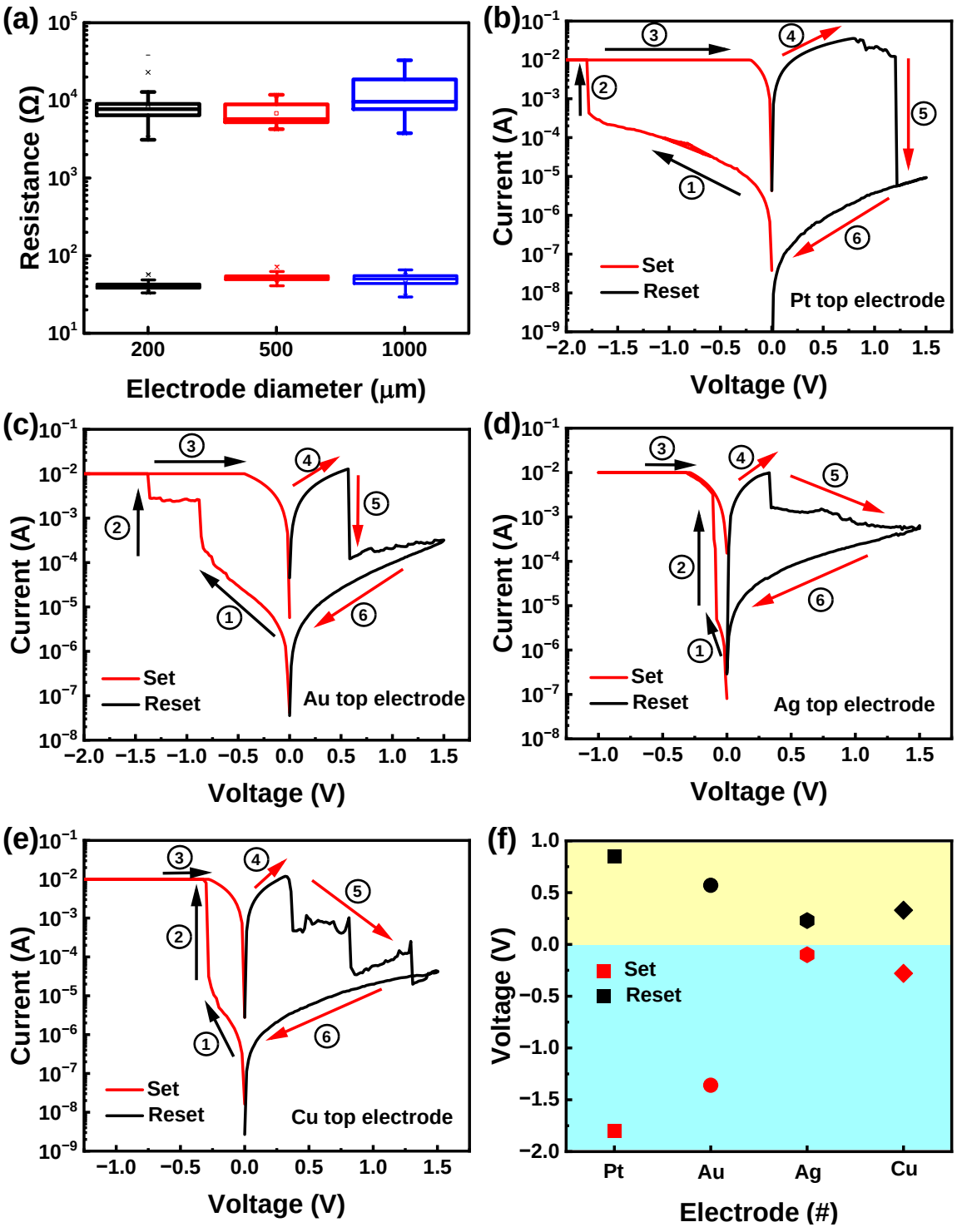

Figure S6. (a) HRS and LRS distribution for different electrode size; Characteristic curves of different top electrodes materials; (b) Pt; (c) Au; (d) Ag; (e) Cu; (f) Set and Reset voltage of different top electrodes.

7. Parameter summary of lead-free perovskite based memristors

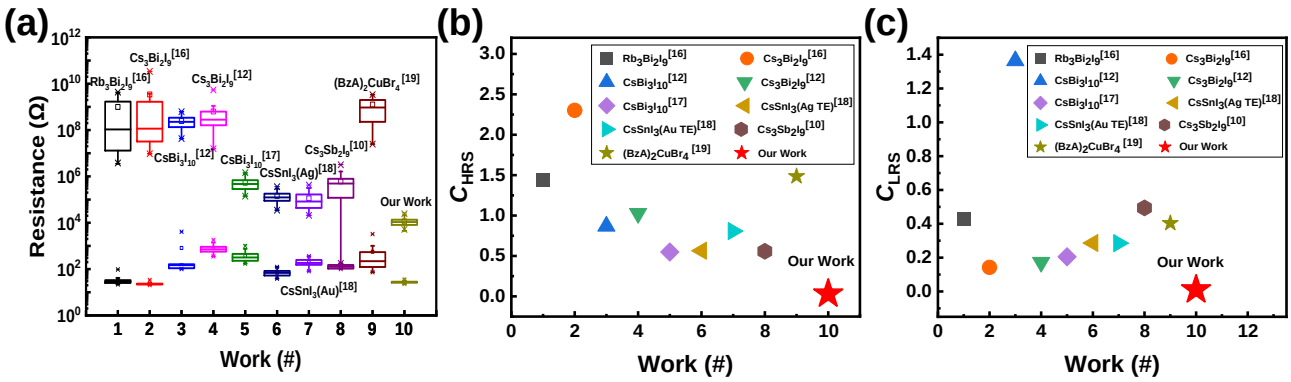

Figure S7. (a) Comparison of the resistance stability with data reported previously; The coefficient of variation of (b) HRS and (c) LRS.

Table S2. Parameters of lead-free perovskite based memristors

Structure	V_{set} **(V)**	V_{reset} **(V)**	**Cycles (#)**	**HRS**	**LRS**	**On/Off Ratio**	**Retention（s）**	**Ref.**
Au/$Rb_3Bi_2I_9$/Pt /Ti/SiO_2/Si	0.09		200	~10^6-10^{10}	~10^2	10^7	~10^3	[16]
Au/$Cs_3Bi_2I_9$/Pt /Ti/SiO_2/Si	0.10		400	~10^7-10^{11}	~10^2	10^7	~10^3	[16]
Ag (AgO_x) /$CsBi_3I_{10}$/FTO	-0.14	0.55	250	~10^7-10^9	~10^3-10^4	≈10^6	< 10^2	[12]
Ag (AgOx) /$Cs_3Bi_2I_9$/FTO	-0.12	1	250	~10^7-10^{11}	~10^2-10^4	≈10^6	< 10^3	[12]
Al/$CsBi_3I_{10}$ /ITO	-1.7	0.9	10^2	~10^5-10^6	~10^2-10^3	10^3	10^4	[17]
Ag/PMMA /$CsSnI_3$/Pt	0.13	-0.08	600	~10^5-10^6	~10^2-10^3	10^3	10^3	[18]
Au/PMMA /$CsSnI_3$/Pt			120	~10^4-10^6	~10^2-10^3	10^2		[18]
Al /$Cs_3Sb_2I_9$ / ITO	0.4	-3.5	＜100	~10^2-10^7	~10^2	10^4	10^4	[10]
Ag/PMMA /$(BzA)_2CuBr_4$ /Pt/Ti/SiO_2/Si	0.21	-0.27	10^3	~10^7-10^{10}	~10^2-10^4	10^8	~10^3	[19]
Ag/$CBL_{0.4}I$ /ITO	**-0.10**	**0.23**	**128**	**~10^4**	**~30**	**10^2**	**10^4**	**Our wok**

8. Cumulative memory effects of Ag/CBL$_{0.4}$I/ITO

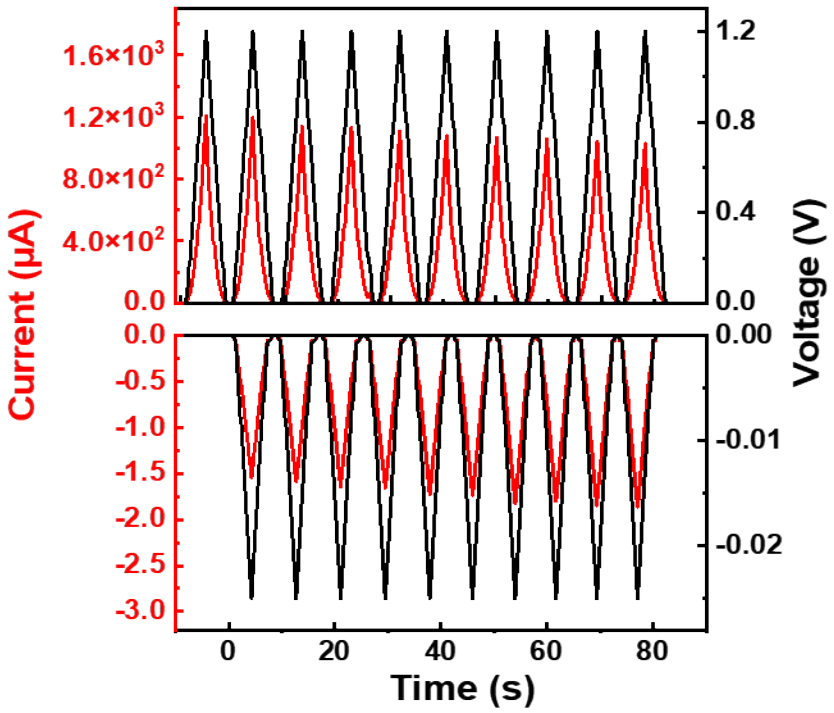

Figure S8. Current and voltage versus time in the positive and negative regions.

9. EPSC behavior of Ag/CBL$_{0.4}$I/ITO

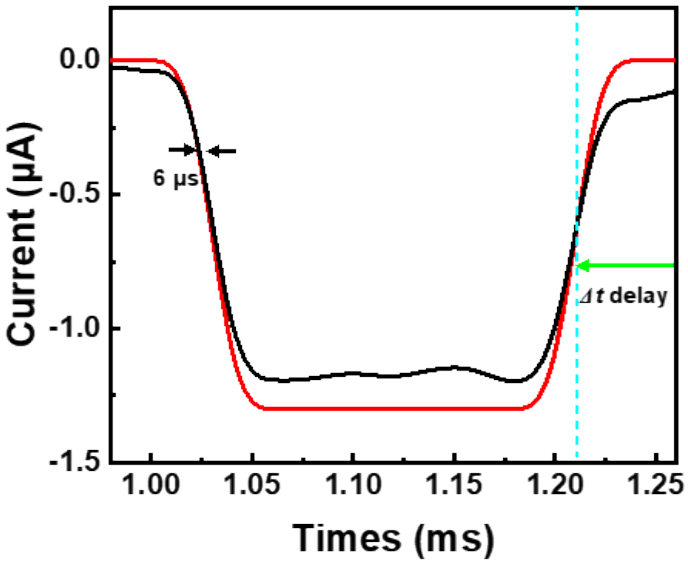

Figure S9. Excitatory postsynaptic current (EPSC) triggered by an electrical pulse with an amplitude of 0.3 V and a width of 200 μs. (A voltage pulse with an applied voltage amplitude of 0.3 V and a pulse width of 200 μs triggered an EPSC of 1.17 μA, resulting in an energy consumption of 70 pJ. The energy consumption is calculated according to the equation: $E = UIt$, where U, I, and t represent the pulse amplitude, EPSC peak value and pulse width, respectively.

10. Summary of energy consumption parameters for perovskite-based synaptic memristors

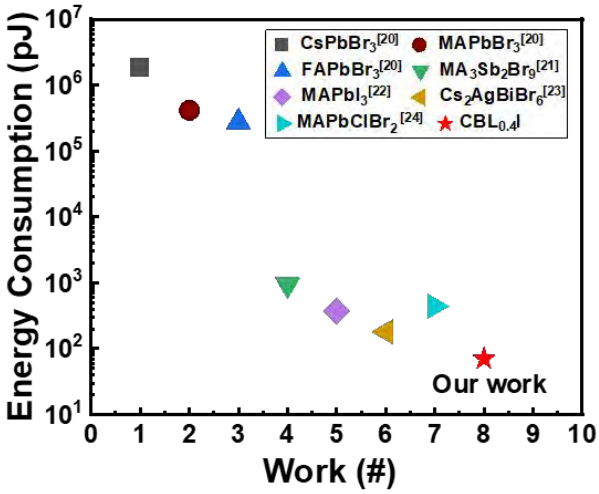

Figure S10. Comparison of the energy consumption/unit area with data reported previously.

Table S3. Energy consumption parameters of perovskite-based synaptic memristors

Structure	Pulse Voltage（V）	Pulse Width（μs）	Energy Consumption (pJ)	Pattern Recognition Accuracy	Ref.
Al/Ca/Bphen/$CsPbBr_3$ /PEDOT:PSS/ITO	3	1×10^4	1.8×10^6	~	[20]
Al/Ca/Bphen/$MAPbBr_3$ /PEDOT:PSS/ITO	3	1×10^4	4.1×10^5	~	[20]
Al/Ca/Bphen/$FAPbBr_3$ /PEDOT:PSS/ITO	3	1×10^4	2.8×10^5	~	[20]
Ag/PMMA/$MA_3Sb_2Br_9$ /ITO	0.05	5×10^2	935	~	[21]
Ag/$MAPbI_3$/FTO	0.9	1×10^2	373	~	[22]
Ag/PMMA/$Cs_2AgBiBr_6$ /ITO	0.3	0.8×10^2	180		[23]
Al/$MAPbClBr_2$/Si	0.5	2.5×10^4	440		[24]
Ag/$CBL_{0.4}$I/ITO	**-0.3**	**2×10^2**	**70**	**94.25%**	**Our work**

References

[1] Blochl, P. E. Projector augmented-wave method. *Phys. Rev. B* **1994**, *50*, 17953-17979, DOI: 10.1103/physrevb.50.17953

[2] Kresse, G.; Joubert, D. From ultrasoft pseudopotentials to the projector augmented-wave method. *Phys. Rev. B* **1999**, *59*, 1758-1775, DOI: 10.1103/PhysRevB.59.1758

[3] Kresse, G.; Furthmu¨ller, J. Efficient iterative schemes for ab initio total-energy calculations using a plane-wave basis set. *Phys. Rev. B* **1996**, *54*, 169-186, DOI: 10.1103/PhysRevB.54.11169

[4] John P. Perdew; Kieron Burke; Ernzerhof, M. Generalized Gradient Approximation Made Simple. *Phys. Rev. Lett.* **1996**, *77*, 3865-3868, DOI: 10.1103/PhysRevLett.77.3865

[5] Heyd, J.; Scuseria, G. E. Assessment and validation of a screened Coulomb hybrid density functional. *J. Chem. Phys.* **2004**, *120*, 7274-7280, DOI: 10.1063/1.1668634

[6] Monkhorst, H. J.; Pack, J. D. Special points for Brillouin-zone integrations. *Phys. Rev. B* **1976**, *13*, 5188-5192, DOI: 10.1103/PhysRevB.13.5188

[7] Luo, F.; Wu, Y.; Tong, J.; Tian, F.; Zhang, X. Resistive Switching and Artificial Synaptic Performances of Memristor based on Low-Dimensional Bismuth Halide Perovskites. *Nano Research* **2022**, DOI: 10.1007/s12274-023-5411-x

[8] Zheng, Y.; Luo, F.; Ruan, L.; Tong, J.; Yan, L.; Sun, C.; Zhang, X. A facile fabrication of lead-free Cs_2NaBiI_6 double perovskite films for memory device

application. *J. Alloys Compd.* **2022**, *909*, 164613, DOI: 10.1016/j.jallcom.2022.164613

[9] Liu, Z.; Tang, H.; Cheng, P.; Kang, R.; Zhou, J.; Zhao, X.; Zhao, J.; Zuo, Z. High-Performance and Environmentally Robust Multilevel Lead-Free Organotin Halide Perovskite Memristors. *Adv. Electron. Mater.* **2022**, *9*, 2201005, DOI: 10.1002/aelm.202201005

[10] Paramanik, S.; Maiti, A.; Chatterjee, S.; Pal, A. J. Large Resistive Switching and Artificial Synaptic Behaviors in Layered $Cs_3Sb_2I_9$ Lead-Free Perovskite Memory Devices. *Adv. Electron. Mater.* **2022**, *8*, 2100237, DOI: 10.1002/aelm.202100237

[11] Gao, Q.; Huang, J.; Gao, J.; Geng, X.; Ji, Y.; Li, H.; Wang, G.; Liang, B.; Wang, M.; Xiao, Z.; Zhu, Y.; Chu, P. K.; Huang, A. Tunable plasticity in functionalized honeycomb synaptic memristor for neurocomputing. *Mater. Today Phys.* **2023**, *30*, 100947, DOI: 10.1016/j.mtphys.2022.100947

[12] Ge, S.; Guan, X.; Wang, Y.; Lin, C.-H.; Cui, Y.; Huang, Y.; Zhang, X.; Zhang, R.; Yang, X.; Wu, T. Low-Dimensional Lead-Free Inorganic Perovskites for Resistive Switching with Ultralow Bias. *Adv. Funct. Mater* **2020**, *30*, 2002110, DOI: 10.1002/adfm.202002110

[13] Kim, S. J.; Lee, T. H.; Yang, J.-M.; Yang, J. W.; Lee, Y. J.; Choi, M.-J.; Lee, S. A.; Suh, J. M.; Kwak, K. J.; Baek, J. H.; Im, I. H.; Lee, D. E.; Kim, J. Y.; Kim, J.; Han, J. S.; Kim, S. Y.; Lee, D.; Park, N.-G.; Jang, H. W. Vertically aligned two-dimensional halide perovskites for reliably operable artificial synapses. *Mater. Today* **2021**, *52*, 19-30, DOI: 10.1016/j.mattod.2021.10.035

[14] Sun, Y.; Tai, M.; Song, C.; Wang, Z.; Yin, J.; Li, F.; Wu, H.; Zeng, F.; Lin, H.; Pan, F. Competition between Metallic and Vacancy Defect Conductive Filaments in a $CH_3NH_3PbI_3$-Based Memory Device. *J. Phys. Chem. C* **2018**, *122*, 6431-6436, DOI: 10.1021/acs.jpcc.7b12817

[15] Li, D.; Dong, X.; Cheng, P.; Song, L.; Wu, Z.; Chen, Y.; Huang, W. Metal Halide Perovskite/Electrode Contacts in Charge-Transporting-Layer-Free Devices. *Adv. Sci.* **2022**, *9*, 2203683, DOI: 10.1002/advs.202203683

[16] Cuhadar, C.; Kim, S. G.; Yang, J. M.; Seo, J. Y.; Lee, D.; Park, N. G. All-Inorganic Bismuth Halide Perovskite-Like Materials $A_3Bi_2I_9$ and $A_3Bi_{1.8}Na_{0.2}I_{8.6}$ (A = Rb and Cs) for Low-Voltage Switching Resistive Memory. *ACS Appl. Mater. Interfaces* **2018**, *10*, 29741-29749, DOI: 10.1021/acsami.8b07103

[17] Xiong, Z.; Hu, W.; She, Y.; Lin, Q.; Hu, L.; Tang, X.; Sun, K. Air-Stable Lead-Free Perovskite Thin Film Based on $CsBi_3I_{10}$ and Its Application in Resistive Switching Devices. *ACS Appl. Mater. Interfaces* **2019**, *11*, 30037-30044, DOI: 10.1021/acsami.9b09080

[18] Han, J. S.; Le, Q. V.; Choi, J.; Kim, H.; Kim, S. G.; Hong, K.; Moon, C. W.; Kim, T. L.; Kim, S. Y.; Jang, H. W. Lead-Free All-Inorganic Cesium Tin Iodide Perovskite for Filamentary and Interface-Type Resistive Switching toward Environment-Friendly and Temperature-Tolerant Nonvolatile Memories. *ACS Appl. Mater. Interfaces* **2019**, *11*, 8155-8163, DOI: 10.1021/acsami.8b15769

[19] Kim, S.-Y.; Yang, J.-M.; Choi, E.-S.; Park, N.-G. Layered $(C_6H_5CH_2NH_3)_2CuBr_4$ Perovskite for Multilevel Storage Resistive Switching Memory. *Adv. Funct. Mater.*

2020, *30*, 2002653, DOI: 10.1002/adfm.202002653

[20] John, R. A.; Yantara, N.; Ng, Y. F.; Narasimman, G.; Mosconi, E.; Meggiolaro, D.; Kulkarni, M. R.; Gopalakrishnan, P. K.; Nguyen, C. A.; De Angelis, F.; Mhaisalkar, S. G.; Basu, A.; Mathews, N. Ionotronic Halide Perovskite Drift-Diffusive Synapses for Low-Power Neuromorphic Computation. *Adv. Mater.* **2018**, *30*, 1805454, DOI: 10.1002/adma.201805454

[21] Yang, J.-M.; Choi, E.-S.; Kim, S.-Y.; Kim, J.-H.; Park, J.-H.; Park, N.-G. Perovskite-related $(CH_3NH_3)_3Sb_2Br_9$ for forming-free memristor and low-energy-consuming neuromorphic computing. *Nanoscale* **2019**, *11*, 6453-6461, DOI: 10.1039/C8NR09918A

[22] Ku, B.; Koo, B.; Sokolov, A. S.; Ko, M. J.; Choi, C. Two-terminal artificial synapse with hybrid organic–inorganic perovskite $(CH_3NH_3)PbI_3$ and low operating power energy (~47 fJ/μm^2). *J. Alloys Compd.* **2020**, *833*, 155064, DOI: 10.1016/j.jallcom.2020.155064

[23] Lao, J.; Xu, W.; Jiang, C.; Zhong, N.; Tian, B.; Lin, H.; Luo, C.; Travas-sejdic, J.; Peng, H.; Duan, C.-G. An air-stable artificial synapse based on a lead-free double perovskite $Cs_2AgBiBr_6$ film for neuromorphic computing. *J. Mater. Chem. C* **2021**, *9*, 5706-5712, DOI: 10.1039/D1TC00655J

[24] Yu, H.; Gong, J.; Wei, H.; Huang, W.; Xu, W. Mixed-halide perovskite for ultrasensitive two-terminal artificial synaptic devices. *Mater. Chem. Front.* **2019**, *3*, 941-947, DOI: 10.1039/C9QM00061E